



A Hierarchical Control Scheme for Active Power-assist Lower-limb Exoskeletons

Jing Deng^{1,2} · Wenzheng Jiang² · Haibo Gao¹ · Yapeng Shi^{1,3}  · Mantian Li⁴

Received: 23 December 2023 / Revised: 22 May 2024 / Accepted: 23 May 2024
© Jilin University 2024

Abstract

Effectively controlling active power-assist lower-limb exoskeletons in a human-in-the-loop manner poses a substantial challenge, demanding an approach that ensures wearer autonomy while seamlessly adapting to diverse wearer needs. This paper introduces a novel hierarchical control scheme comprising five integral components: intention recognition layer, dynamics feedforward layer, force distribution layer, feedback compensation layer, as well as sensors and actuators. The intention recognition layer predicts the wearer's movement and enables wearer-dominant movement through integrated force and position sensors. The force distribution layer effectively resolves the statically indeterminate problem in the context of double-foot support, showcasing flexible control modes. The dynamics feedforward layer mitigates the effect of the exoskeleton itself on movement. Meanwhile, the feedback compensation layer provides reliable closed-loop control. This approach mitigates abrupt changes in joint torques during frequent transitions between swing and stance phases by decomposed dynamics. Validating this innovative hierarchical control scheme on a hydraulic exoskeleton platform through a series of experiments, the results demonstrate its capability to deliver assistance in various modes such as stepping, squatting, and jumping while adapting seamlessly to different terrains.

Keywords Hierarchical control · Active power-assist · Exoskeleton robots · Dynamics feedforward · Force distribution · Feedback compensation

1 . Introduction

Active power-assist exoskeleton robots are specialized wearable robots worn by humans that can enhance human physical capabilities. These exoskeletons seamlessly integrate human intelligence and agility with the high load-bearing capacity and powerful dynamics of robots. The coupled human–robot system empowers wearers with remarkable mobility and operational capabilities [1, 2]. The applications of such active assistive exoskeletons span various domains,

including rehabilitation therapy, industrial production, and individual soldier devices, showcasing significant potential for widespread applications [3].

Exoskeletons are typically classified into three main categories based on the specific body parts they are designed to assist: full-body exoskeletons, upper-limb exoskeletons, and lower-limb exoskeletons [4]. There are several reasons why lower-limb exoskeletons hold a more important role in comparison. First, the lower-limb exoskeletons bear the majority of the body's weight and are critical to mobility. Second, lower-limb exoskeletons can play an important role in rehabilitation efforts for those who have difficulty walking or recovering from injuries. By focusing on lower limb assistance, exoskeletons can directly address issues related to mobility impairments and enhance an individual's athleticism [5]. The human lower limb consists of three primary joints, namely the ankle joint, knee joint, and hip joint. In the robotics community, the Degrees of Freedom (DoF) of the lower limb are often simplified to seven DoFs, with three in the hip joint, one in the knee joint, and three in the ankle

✉ Yapeng Shi
shi.yapeng@hit.edu.cn

¹ State Key Laboratory of Robotics and System, Harbin Institute of Technology, Harbin 150001, Heilongjiang, China

² Shenzhen Academy of Aerospace Technology, Shenzhen 518063, China

³ Faculty of Computing, Harbin Institute of Technology, Harbin 150001, Heilongjiang, China

⁴ Institute of Intelligent Manufacturing Technology, Shenzhen Polytechnic University, Shenzhen 518055, China

joint. Lower limb exoskeletons are currently a hot topic of research [3].

Pre-programming techniques have found widespread application in rehabilitation training exoskeletons. These methodologies involve the collection of gait trajectories from normal walking, which are then utilized to establish a gait database [6]. Subsequently, the gathered trajectories can be employed for passive rehabilitation training for patients who have either completely or partially lost their lower limb mobility [7]. Some researchers have incorporated concepts from the field of legged robotics, such as Capture Point (CP), Divergent Component of Motion (DCM), and Zero-Moment Point (ZMP), to enhance the balance restoration capabilities of exoskeletons [8]. However, this approach fails to align seamlessly with the natural movement patterns of the healthy wearers and may even introduce issues conflicting with human motion [9].

Achieving human–machine coupling assistance perfectly with human movement poses a significant challenge faced by exoskeleton control [10]. The difficulty arises from the fact that the motion of individuals is inherently variable and difficult to predict, influenced by factors such as the unique characteristics of different wearers, diverse terrains, and the varying trajectories associated with different actions. Gait recognition and phase identification technologies [11–13] aim to categorize human gait into different patterns such as walking, running, ascending or descending stairs, etc. Subsequently, the information further segments a gait cycle into phases such as swing initiation, swing termination, and support initiation.

The collection and decoding of physiological signals constitute commonly employed methods for perceiving human movement intentions. The bioelectric signal sources mainly include Surface ElectroMyoGraphy (sEMG) and Electro-EncephaloGraphy (EEG) [14]. sEMG, characterized by its simplicity, timeliness, and fidelity, has been widely applied for recognition in the field of lower limb exoskeleton robots [15]. EEG-based recognition methods utilize scalp electrodes placed close to the motor cortex functional areas of the brain, which can collect EEG containing specific thought activities when the brain is conceiving a motor plan. Decoding these signals allows for the recognition of specific movement intentions [16]. Compared to the single utilization of EEG or sEMG, the integration of these two physiological signals through data fusion may predict a more comprehensive human motion intent [17]. Subsequently, Kalman filters, Bayesian fusion, and other multimodal signal fusion technologies integrate these two physiological signals into controllers [18, 19]. [20] proposed a novel hierarchical control used sEMG-based intention estimation, mid-level strength regulation, and low-level actuator. The effectiveness of the exoskeleton assistance has been validated via shoulder joint elevation experiments. However, these methods are

susceptible to factors such as electrode–skin contact impedance, electrode placement, interference from surrounding muscle signals, and muscle or brain fatigue. This inevitably requires frequent calibration and can also cause inconvenience when arranging electrode wires on the human body [21].

To tackle this problem, an effective approach relies on human–machine interaction data, specifically Ground Reaction Forces (GRFs), human joint trajectories, interaction forces, IMU, and other non-bioelectric signals [22]. Nevertheless, these methods encounter notable limitations, such as time delays, which consequently influence the latency in assistive control. Human-exoskeleton (H.-E.) collaborative control strategies, such as hybrid impedance control, adaptive impedance control, hybrid impedance-sliding mode control, and neural learning impedance control, ensure safety and comfort [23–27].

However, the model-based control methods face challenges in adapting to changes in payload and external environments. Likewise, trajectory tracking methods, even with sophisticated impedance control techniques, prove inadequate for significant wearer-induced changes in multimodal locomotion, such as walking, squatting, and jumping. [28] developed a mid-level controller that considers the dynamics of the exoskeleton and external loads. The controller has the potential to adapt to multimodal motions and various external loads, provided that long-term experiments are carried out. However, the vibration of the exoskeleton during experiments poses a potential risk of injuries to the wearer, particularly among vulnerable populations such as women and the elderly, especially in the case of hydraulic exoskeletons.

In response to these challenges, this paper introduces a novel control framework for power-assistant exoskeleton robots, encompassing an intention recognition layer, a dynamics feedforward layer, a force distribution layer, a feedback compensation layer, along with sensors and actuators. A series of the experiments have been carried out and the results of data analysis demonstrate the performance of the proposed active power-assist exoskeletons.

The innovative contributions of this work can be summarized as follows:

- The proposed hierarchical control architecture eliminates the necessity of depending on unreliable physiological signals feedback from the wearer. Instead, it accurately perceives the wearer's motion intentions through feedback from force and position sensors integrated into the exoskeleton.
- Leveraging decomposed single-leg dynamics and backpack dynamics, joint torque calculations are based on exoskeleton inertia and contact force measurements. This mitigates abrupt changes in joint torques caused by frequent transitions between swing and stance phases.

- The force distribution layer effectively addresses the statically indeterminate problem in the case of double-foot support.
- The independence of each component within the hierarchical control architecture facilitates seamless transitions between no-powered mode, follow-up mode, and active assistance mode for the exoskeletons.

The remainder of this paper is organized as follows: Sect. 2 provides an in-depth exploration of the overall hierarchical control architecture, delineating the various layers and their functionalities. Following this, Sect. 3 delves into the detailed implementation processes of each layer, focusing on the intent perception, dynamic feedforward, force distribution, feedback compensation layers, sensors and actuators. Section 4 presents the experimental setup, methodologies, and a thorough analysis of the obtained results. Finally, the paper concludes with a comprehensive summary of the proposed control scheme and future work.

2 Overall Architecture

The exoskeleton architecture of the H.-E. coupling system is illustrated in Fig. 1. There are two controllers in this H.-E. coupled system, one is the human brain and the other is the controller of the exoskeleton robot. The human brain functions as a sensory input processor, utilizing mechanisms such as the cochlea/inner ear, vision, and touch to perceive the body's movements. It generates nerve impulses that drive muscles towards desired states. Simultaneously, the exoskeleton robot assumes the role of assisting the human body. Initiating the H.-E. coupling mechanism, a kinematic relationship with the human body is established. Subsequently, the integrated sensing system mounted on the exoskeleton collects motion data and interface forces exerted by the wearer.

These signals are substituted into the equation of motion of the human dynamic model to calculate the required forces (which is defined as the intention recognition). The resulting torques, multiplied by an assistive factor, are applied to the corresponding joints to mitigate the joint torque contribution from the human body.

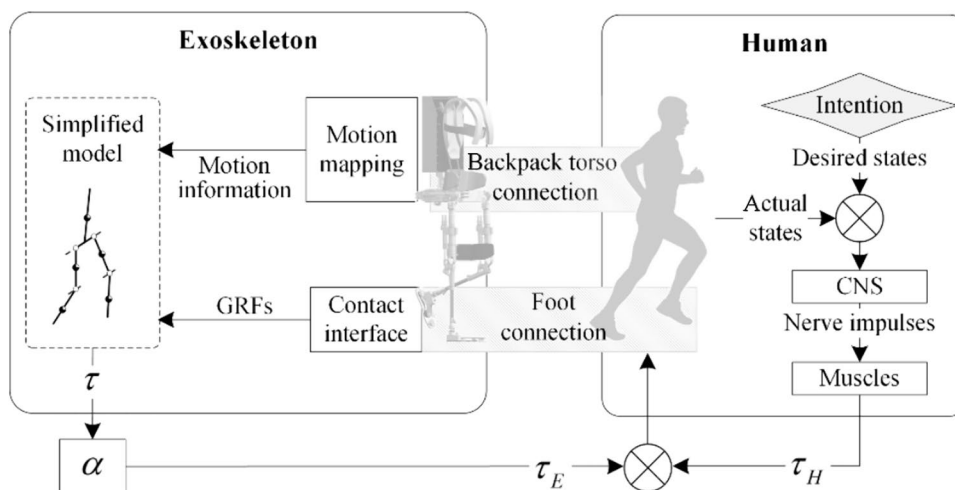
Figure 2 illustrates a H.-E. hierarchical control scheme proposed in this paper for active power-assist exoskeletons.

The scheme comprises five integral components: intention recognition layer, dynamics feedforward layer, feedback compensation layer, force distribution layer, as well as sensors and actuators. The intention recognition layer is tasked with acquiring pertinent human motion information from an array of sensors and subsequently outputting the expected H.-E. interface forces. The dynamics feedforward layer retrieves the exoskeleton motion data from proprioceptors, generating feedforward joint torques for the exoskeleton's swing leg and support forces for the backpack. The feedback compensation layer differentiates between the expected H.-E. foot-end and torso interface forces, as obtained from the intention recognition layer, and the actual H.-E. interface forces measured by the sensors. It applies Proportional Integral Derivative (PID) regulation based on the deviation signal.

Subsequently, the force distribution layer seeks to sum up to torso compensation forces provided by the feedback compensation layer and the required backpack support forces from the dynamics feedforward layer. Referencing the target H.-E. interface forces, as derived from the intention perception layer, the resultant forces are distributed to the target support forces for each hip joint. The target support forces for both left and right hips, in conjunction with foot-end compensation forces, are then translated into joint torques for the exoskeleton.

The control loop responsible for governing these torques undergoes switching based on contact states, ensuring

Fig. 1 The exoskeleton architecture represents the coupling system between the exoskeleton and the wearer. The connection is established through coupling points located at the backpack-torso junction and the foot-end, providing dynamic assistance to the wearer



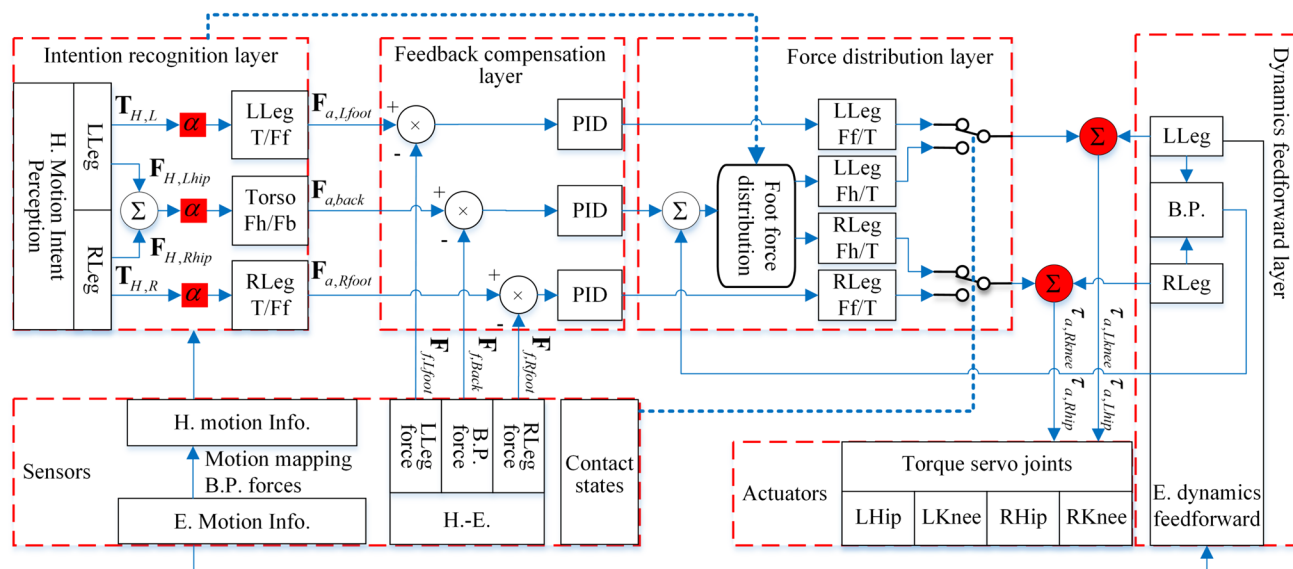


Fig. 2 H.-E. hierarchical control scheme for active power-assist exoskeletons. The red curved boxes outline each layer of the hierarchical control scheme, while the blue solid lines represent the transmission

of variable information, and the blue dashed lines indicate finite state transitions (*E.* for exoskeleton, *H.* for human, *B.P.* for backpack, *L* for left, *R* for right)

seamless transitions between various modes of operation. Through the summation of feedforward torques, the exoskeleton's joint torque commands are executed with precision by the hydraulic drive units, thereby guaranteeing robust and responsive assistance to the wearer.

3 Hierarchical Control Scheme Details

3.1 Intention Recognition Layer

According to the Adaptive Model Theory (AMT) proposed by Neilson [29], the human brain pre-plans limb motion trajectories according to action intentions. These trajectories are then translated by the central nervous system's dynamic model into a sequence of nerve pulses that control each muscle group in real-time. AMT's fundamental assumption is that the neural system can adaptively remember and simulate the inverse dynamic characteristics of the human body. Based on this set of neural networks that have been repeatedly trained and corrected, the human brain can convert the expected limb motion trajectory into a neural pulse sequence that controls the coordinated movement of each muscle group. Through a set of neural networks that have undergone repeated training and correction, the brain can convert anticipated limb motion trajectories into neural pulse sequences that coordinate each muscle group's movement. With extended training and reinforcement, the control accuracy of the brain progressively enhances, facilitating the execution of more precise and refined movements. Research demonstrates that AMT reliably simulates human motion.

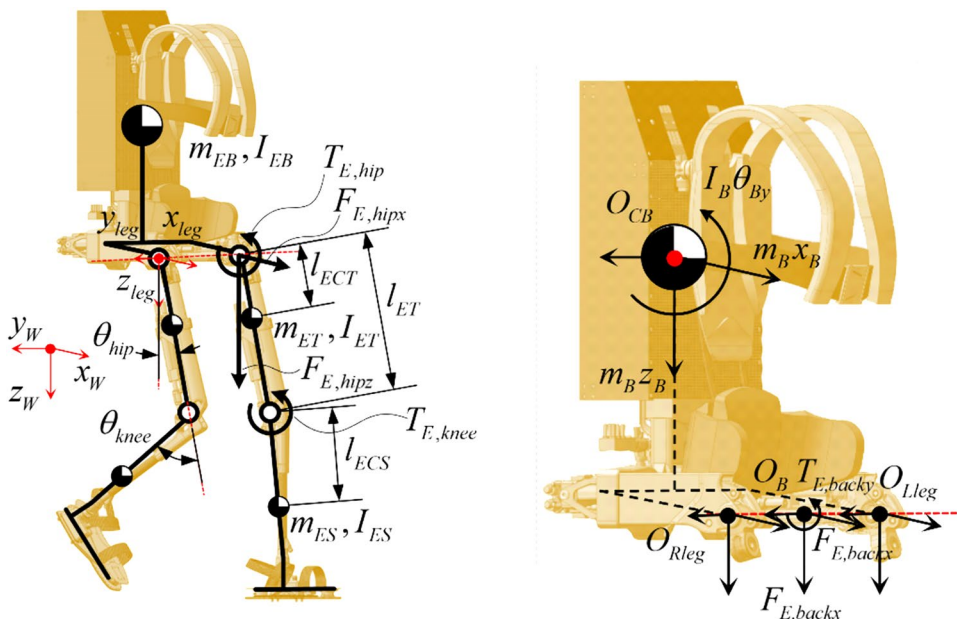
Inspired by the AMT, we introduce a method for deducing human motion intentions in reverse by utilizing a human inverse dynamics model. This approach entails establishing a normalized inverse dynamics model of the human body, which can be used to solve the torque of each human joint by substituting the posture information and joint motion information. The joint torques provide an accurate, real-time reflection of the body's motion tendencies. We have comprehensively discussed this research work in our previous paper [3].

3.2 Dynamics Feedforward Layer

The establishment of an inverse dynamics model for the exoskeleton's leg aims to acquire the torques $T_{E,hip}$ and $T_{E,knee}$ required at the hip and knee joints during the swing motion, as well as the forces $F_{E,hipx}$ and $F_{E,hipz}$ exerted by the swing leg on the exoskeleton's hip joint. The origin of the coordinate system for the single leg is set at the intersection of the thigh axis and the hip joint flexion–extension axis, with the direction of the coordinate axes as depicted in Fig. 3.

During leg swinging, the hydraulic cylinder on the thigh undergoes only small-scale rotation, and its mass is relatively small. Therefore, the motion of the hydraulic cylinder and piston rod is ignored. A high-stiffness elastic constraint is applied to the ankle joint, which remains essentially relatively stationary during the swing phase, allowing the foot and lower leg to be treated as a single link. This simplification results in a two-link pendulum swing model, with the mass of the thigh component denoted as m_{ET} , its moment of inertia about the Center of Mass (CoM) as I_{ET} , the mass of

Fig. 3 Simplified 5-link model and floating-based backpack of the exoskeleton robot



the lower leg component as m_{ES} , and its moment of inertia as I_{ES} . The distance from the thigh’s CoM to the hip joint is denoted as l_{ECT} , the length of the thigh as l_{ET} , and the distance from the CoM of the lower leg to the knee joint as l_{ECS} .

Given that the hip joint moves with the body, the inverse dynamics model of the swing leg can be regarded as a planar two-link mechanism with a floating base. In this work, Lagrangian mechanics is adopted for modeling, following a process similar to that of human single-leg inverse dynamics, which is presented in [10]. The main difference lies in calculating the terms $F_{E,hipx}$ and $F_{E,hipz}$. Using the Lagrange approach, we have:

$$\begin{cases} F_{E,hipx} = \frac{d}{dt} \left[\frac{\partial(K_{leg} - P_{leg})}{\partial \dot{x}_{leg}} \right] - \frac{\partial(K_{leg} - P_{leg})}{\partial x_{leg}} \\ F_{E,hipz} = \frac{d}{dt} \left[\frac{\partial(K_{leg} - P_{leg})}{\partial \dot{z}_{leg}} \right] - \frac{\partial(K_{leg} - P_{leg})}{\partial z_{leg}} \end{cases} \quad (1)$$

where K_{leg} and P_{leg} represent the kinetic and potential energies of a single leg, respectively. It's important to note that we didn't make a deliberate distinction between the swing phase and stance phase here. In reality, the difference between the swing phase and stance phase lies solely in the presence or absence of GRFs at the foot-end. In the inverse dynamic equations of the rigid body system, each component of joint torque satisfies the principle of linear superposition. Consequently, the aforementioned process yields joint torques and hip joint forces without considering the GRFs.

Assuming the position of the center of mass (CoM) in the backpack coordinate system is denoted as $P_{CB} = \{x_{CB}, y_{CB}, z_{CB}\}$, with the coordinates of the left and right hip joints denoted as $P_{LK} = \{0, y_{LK}, 0\}$ and

$P_{RK} = \{0, y_{RK}, 0\}$, respectively. Thereby, we can determine the resulting force required to maintain the posture and movement of the exoskeleton backpack, which can be expressed as follows:

$$\begin{cases} F_{E,backx} = -m_B \ddot{x}_B + F_{E,Lhipx} + F_{E,Rhipx} \\ F_{E,backz} = -m_B \ddot{z}_B + F_{E,Lhipz} + F_{E,Rhipz} \end{cases} \quad (2)$$

The required torque around y-axis can be expressed as:

$$T_{E,backy} = I_B \ddot{\theta}_{By} - m_B \ddot{x}_B z_{CB} + m_B \ddot{z}_B x_{CB} + T_{E,Lhipy} + T_{E,Rhipy} \quad (3)$$

3.3 Force Distribution Layer

The exoskeleton’s backpack dynamic feedforward provides the forces required to maintain the exoskeleton's posture and movement. These feedforward forces, combined with the corrective forces for the backpack, yield the total forces that the backpack should receive from the exoskeleton's legs. The exoskeleton's two legs simultaneously support the backpack causing an issue of over-determination, making it impossible to determine the individual forces applied by the left and right legs of the exoskeleton. To address this problem, a force distribution approach is designed. The distribution approach is to match the expected resultant force from both legs as closely as possible while satisfying the constraint of physical laws.

Starting with an analysis of the influence on backpack posture, the forces exerted by the legs on both sides in the z-direction cause a roll torque on the backpack, while forces in the x-direction induce yaw torque, and y-torque controls

the pitch of the backpack. Since the backpack is connected to the human torso, adjustments to the human body's posture simultaneously affect the posture of the exoskeleton backpack. Secondly, it is crucial to avoid opposition between the exoskeleton's output and the human body. Specifically, the direction of the force distributed to each stance leg should align with the direction of the force applied by the human leg. Additionally, abrupt changes in leg target forces during the stance/swing phase transition should be avoided. For instance, when one leg switches from the stance phase to the swing phase, if it continues to bear support forces, the wearer will be unable to lift their leg. Therefore, foot force distribution also needs to coordinate with the human gait. Finally, the horizontal force carried out on the stance foot-end is provided by ground friction, and the magnitude of the horizontal force should be limited to prevent slipping. In summary, the following foot-end force distribution principles are proposed: (1) The combined forces from both legs should align with the required total forces as closely as possible; (2) Force should only be distributed to the leg whose force direction aligns with that of the human leg; (3) The ZMP in the x and z directions should align with the zero torque points of the leg's force on the torso; (4) Consideration of the frictional force limit when calculating the torques about the y -axis.

During walking, the backpack is primarily influenced by gravitational acceleration, resulting in a need for significant support force in the z -direction, while the x -direction experiences mainly forward acceleration, making it relatively smaller. Therefore, priority is given to ensuring force distribution in the z -direction. The direction of the force is assessed first: when the force of the left leg $F_{H,Lhipz}$ is in the same direction as F_{sumz} , while the force of the right leg $F_{H,Rhipz}$ is in the opposite direction as F_{sumz} , the total forces are distributed to the left leg:

$$\begin{cases} F_{a,Lhipz} = F_{sumz} \\ F_{a,Rhipz} = 0 \end{cases} \quad (4)$$

On the contrary, when the direction of the $F_{H,Lhipz}$ is opposite to F_{sumz} , while the $F_{H,Rhipz}$ and F_{sumz} are in the same direction, distributed the total forces to the right leg:

$$\begin{cases} F_{a,Lhipz} = 0 \\ F_{a,Rhipz} = F_{sumz} \end{cases} \quad (5)$$

Conversely, when both $F_{H,Lhipz}$, $F_{H,Rhipz}$ and F_{sumz} align with opposite directions, it indicates a conflict between the support force required by the exoskeleton backpack and that required by the human body. To avoid internal force antagonism between the exoskeleton and the wearer, both leg forces are assigned a value of zero. When both $F_{H,Lhipz}$, $F_{H,Rhipz}$ and F_{sumz} align in the same direction, following the coincidence

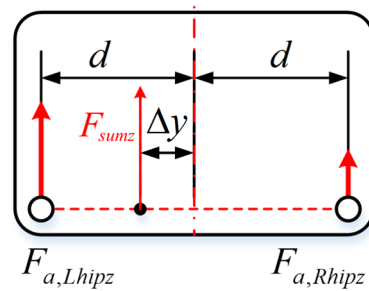


Fig. 4 ZMP of the GRFs with double support feet

of the zero torque points for the exoskeleton and the human, as illustrated in Fig. 4.

With

$$\begin{cases} F_{H,Lhipz}(d - \Delta y) = F_{H,Rhipz}(d - \Delta y) \\ F_{a,Lhipz}(d - \Delta y) = F_{a,Rhipz}(d - \Delta y) \\ F_{a,Lhipz} + F_{a,Rhipz} = F_{sumz} \end{cases} \quad (6)$$

Thereby

$$\begin{cases} F_{a,Lhipz} = \frac{F_{H,Lhipz}}{F_{H,Lhipz} + F_{H,Rhipz}} F_{sumz} \\ F_{a,Rhipz} = \frac{F_{H,Rhipz}}{F_{H,Lhipz} + F_{H,Rhipz}} F_{sumz} \end{cases} \quad (7)$$

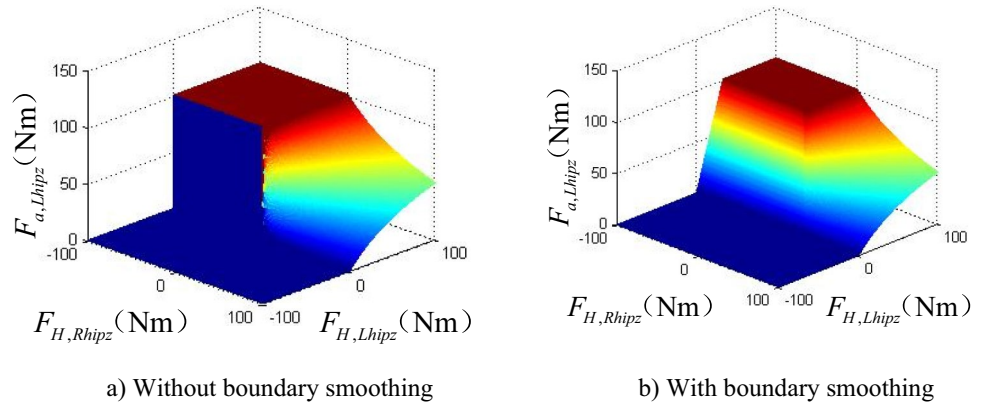
To validate the effectiveness of foot force distribution, assuming $\{F_{H,Lhipz}, F_{H,Rhipz}\} \in [-100, 100]$, $F_{sumz} \equiv 100$. the z -direction force of the left leg is plotted, as depicted in Fig. 5. It can be observed that $F_{a,Lhipz}$ occurs a discontinuity between 0 and 100Nm when $F_{H,Rhipz} < 0$ and $F_{H,Lhipz} \Rightarrow 0$, resulting in severe trembling in the implementation. To prevent abrupt changes caused by such scenarios, the amplitude of $F_{a,Lhipz}$ is artificially limited with $F_{a,Lhipz} < kF_{H,Lhipz}$, achieving a smooth transition at the boundary. The allocation results shown in Fig. 5 are obtained with $k=3$.

The pitch torque is primarily induced by the offset between the exoskeleton backpack's CoM and the human body's CoM. The main consideration in pitch torque distribution is to prevent slippage at the foot-end. The maximum static frictional force that the exoskeleton can provide is denoted as:

$$F_{max} = \mu F_N \quad (8)$$

where μ is the friction coefficient, F_N is the normal forces on the exoskeleton's foot-end. The normal forces on the exoskeleton foot-end are approximately equal to the sum of the human foot-end forces and the z -direction force distributed to one side of the exoskeleton leg. Taking the left foot-end

Fig. 5 Effect of foot force distribution



as an example, $F_{NL} = F_{f,Lhipz} + F_{a,Lhipz}$. Because the friction coefficient of the foot-end is unknown. To ensure both feet have a considerable frictional force margin, the distribution is based on the ratio of normal forces on the left and right foot-end, which yields:

$$\begin{cases} \tau_{a,Lhipy} = \frac{F_{NL}}{F_{NL} + F_{NR}} \tau_{sumy} \\ \tau_{a,Rhipy} = \frac{F_{NR}}{F_{NL} + F_{NR}} \tau_{sumy} \end{cases} \quad (9)$$

From Fig. 5, it can be observed that when the force $F_{H,hipz}$ exerted by one side of the human leg approaches zero, both $F_{a,hipz}$ and $\tau_{a,hipy}$ tend towards zero. Consequently, the target load on the exoskeleton leg decreases to zero before transitioning from the stance to the swing phase. This naturally initiates the swing state. The force distribution method in the x-direction is consistent with that in the z-direction.

3.4 Feedback Compensation Layer

The active assistance for the swing leg is aimed at reducing the energy expenditure for the wearer during leg lifting and

swinging. The leg is suspended on the torso through the hip joint. The gravitational and inertial forces acting on the swing leg are borne by the torso. The loads resulting from the leg's links are transmitted upward along the leg, sequentially inducing forces and torques at the ankle, knee, and hip joints. Therefore, establishing a force transmission pathway from the foot-end to the hip joint can enable assistance for the swing leg.

Most actively assisted exoskeletons directly couple the actuation joints in parallel with the corresponding joints on the human body to provide joint torque assistance. In contrast, this paper proposes a feedback compensation assistance approach that differs from parallel actuation, specifically targeting only the foot-end as the sole coupling point between the human leg and the exoskeleton. This method assists the wearer in lifting and swinging the leg by lifting the foot. The force analysis of the human-in-the-loop exoskeleton robot is depicted in Fig. 6.

Because the H.-E. coupling mechanism ensures a unique motion mapping relationship between the human and exoskeleton, even in situations where the human is completely passive, the exoskeleton robot can still guide the human's

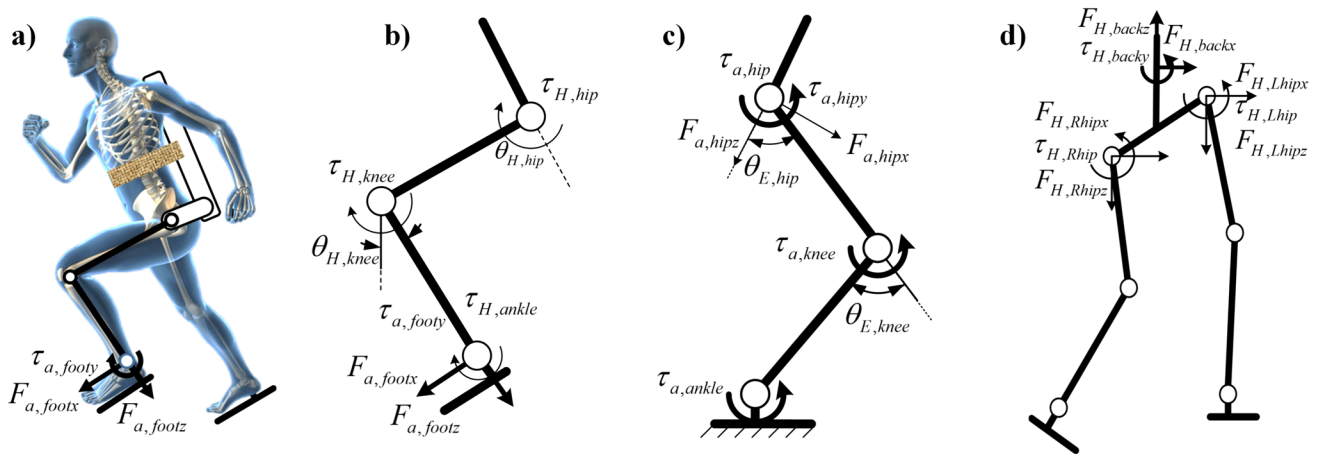


Fig. 6 The force analysis of the human-in-the-loop exoskeleton robot

foot to achieve arbitrary leg lifting and swinging motions. This implies that the assistance method can effectively substitute or partially substitute for the function of human muscles. Separating the feedback compensation control loop of the swing phase from the overall architecture yields the structure depicted in Fig. 7.

In implementation, the torques at each joint obtained from the intention recognition layer is first multiplied by the assistance coefficient α and then mapped to an equivalent foot contact force. By establishing a force balance equation based on the leg configuration, the target GRFs at the foot-end are derived as follows:

$$\begin{cases} F_{a,footx} = \alpha \frac{\tau_{H,knee} - \tau_{H,ankle}}{l_S} \\ \tau_{a,footy} = \alpha \tau_{H,ankle} \\ F_{a,footz} = \alpha \frac{l_S(\tau_{H,hip} - \tau_{H,ankle}) - (\tau_{H,knee} - \tau_{H,ankle})(l_S + l_T \cos \theta_{H,knee})}{l_T \sin \theta_{H,knee}} \end{cases} \quad (10)$$

The individual components of the target GRFs are compared with the corresponding components of the measured GRFs. The deviations are rectified using a PID control approach. Since each component is independent, and the forward channel transfer functions differ, distinct PID parameters G_{Fx} , G_{Fz} and $G_{\tau y}$ are applied for feedback correction in the x , z directions contact forces and y direction torque, respectively. The output of the PID control is the correction amount for the foot contact force, which needs to be converted into control inputs for each joint of the exoskeleton to control its motion. Based on the exoskeleton leg configuration, the corrective torques for each joint of the exoskeleton can be obtained as follows:

$$\begin{cases} \Delta \tau_{ankle} = \Delta \tau_y \\ \Delta \tau_{knee} = \Delta \tau_y + \Delta F_x \\ \Delta \tau_{hip} = \Delta \tau_y + \Delta F_x(l_S + l_T \cos \theta_{E,knee}) + \Delta F_z l_T \sin \theta_{E,knee} \end{cases} \quad (11)$$

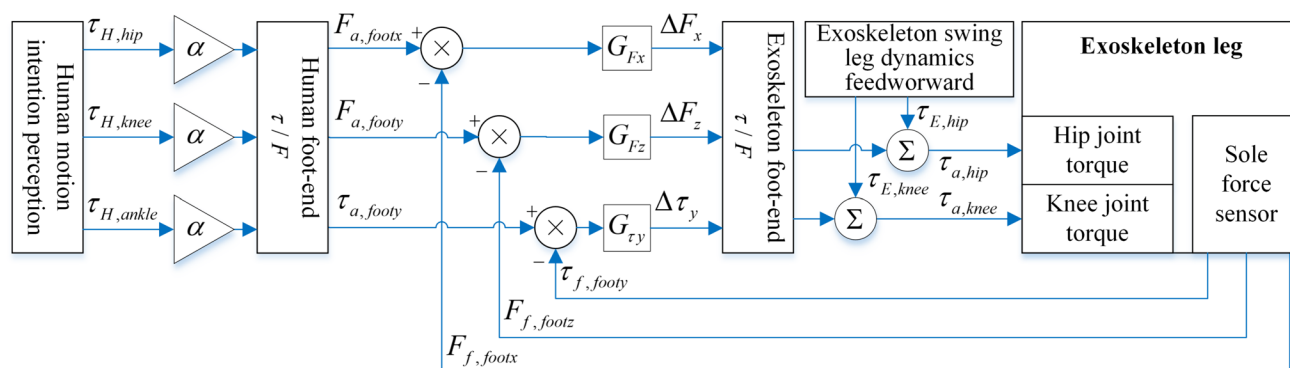


Fig. 7 Feedback compensation diagram of the swing leg

The corrective torques, when superimposed with the feed-forward torques from the exoskeleton single-leg dynamics, result in the target command torques for the exoskeleton joints:

$$\begin{cases} \tau_{a,hip} = \tau_{E,hip} + \Delta \tau_{hip} \\ \tau_{a,knee} = \tau_{E,knee} + \Delta \tau_{knee} \end{cases} \quad (12)$$

This work does not incorporate an actuated unit at the ankle joint. Instead, it is configured as a passive elastic joint. Consequently, it cannot be guaranteed that the actual output torque of the exoskeleton's ankle joint will match the required torque. In such instances, the residual torques must be borne by the human body.

In the feedback compensation layer of the swing leg, the foot-end GRFs can dynamically adjust the joint torques in real-time based on deviations, suppressing disturbances caused by factors such as exoskeleton dynamics feedforward errors, joint torque servo errors, and joint friction. This ensures the accurate realization of the target contact force, thereby guaranteeing the effectiveness of active assistance.

The role of the stance phase is to support the torso of the exoskeleton and the wearer, as well as adjust its posture. From the perspective of mechanical principles, the stance leg establishes a force transmission pathway from the torso to the ground. The load during the stance phase is primarily caused by the torso. Therefore, establishing a bypass for force transmission from the torso to the ground allows for assistance to the support leg. In this study, the exoskeleton's torso is rigidly attached to the human torso. The exoskeleton lifts the human torso through straps on the exoskeleton's backpack, thereby reducing the load on the human's support leg. The control logic for the stance phase is as follows: referencing the forces exerted by the human leg on the torso through the hip joints, the exoskeleton applies proportionate forces to the human torso through the backpack, as illustrated in Fig. 6 d).

Separating the feedback compensation control loop of the stance phase from the overall architecture yields the structure depicted in Fig. 8.

The resultant force exerted on the torso can be directly obtained by summing the forces from both the left and right legs. Multiplying an assistance coefficient yields the target backpack forces applied to the human body:

$$\begin{cases} \tau_{a,backy} = \alpha(\tau_{H,Lhip} + \tau_{H,Rhip}) \\ F_{a,backx} = \alpha(F_{H,Lhipx} + F_{H,Rhipx}) \\ F_{a,backz} = \alpha(F_{H,Lhipz} + F_{H,Rhipz}) \end{cases} \quad (13)$$

Discrepancies between the components of the measured backpack force and those of the target backpack force are corrected using a PID control method. The corrective forces are carried out via feedback correction coefficients. The coefficients in the x and z directions, as well as the y -direction torque, are denoted as G_{Fbx} , G_{Fbz} and $G_{\tau by}$, respectively:

$$\begin{cases} \Delta\tau_{backy} = G_{\tau by}(\tau_{H,backy} - \tau_{f,backy}) \\ \Delta F_{backx} = G_{Fbx}(F_{H,backx} - F_{f,backx}) \\ \Delta F_{backz} = G_{Fbz}(F_{H,backz} - F_{f,backz}) \end{cases} \quad (14)$$

These corrective forces are integrated with the exoskeleton backpack's feedforward forces. Subsequently, the target support forces acting on the exoskeleton's hip joints $F_{a,Lhip} = \{F_{a,Lhipx}, F_{a,Lhipz}, \tau_{a,Lhipy}\}$ and $F_{a,Rhip} = \{F_{a,Rhipx}, F_{a,Rhipz}, \tau_{a,Rhipy}\}$ are determined through the proposed force distribution. These target support forces are then translated into the joint torques for the exoskeleton's

leg, yielding the target torques for each joint during the support phase, as illustrated in Fig. 6.

Considering the configuration of the exoskeleton's leg, we treat the exoskeleton foot as rigidly connected to the ground. The target joint torques for the left legs are as follows:

$$\begin{cases} \tau_{a,Lhip} = -\tau_{a,Lhipy} \\ \tau_{a,Lknee} = \tau_{a,Lhip} + F_{a,Lhipx}l_{ET} \cos \theta_{E,Lhip} \\ - F_{a,Lhipz}l_{ET} \sin \theta_{E,Lhip} \\ \tau_{a,Lankle} = \tau_{a,Lknee} \\ + F_{a,Lhipx}l_{ES} \cos(\theta_{E,Lknee} - \theta_{E,Lhip}) \\ + F_{a,Lhipz}l_{ES} \sin(\theta_{E,Lknee} - \theta_{E,Lhip}) \end{cases} \quad (15)$$

The right leg joint torques are as follows:

$$\begin{cases} \tau_{a,Rhip} = -\tau_{a,Rhipy} \\ \tau_{a,Rknee} = \tau_{a,Rhip} + F_{a,Rhipx}l_{ET} \cos \theta_{E,Rhip} \\ - F_{a,Rhipz}l_{ET} \sin \theta_{E,Rhip} \\ \tau_{a,Rankle} = \tau_{a,Rknee} \\ + F_{a,Rhipx}l_{ES} \cos(\theta_{E,Rknee} - \theta_{E,Rhip}) \\ + F_{a,Rhipz}l_{ES} \sin(\theta_{E,Rknee} - \theta_{E,Rhip}) \end{cases} \quad (16)$$

3.5 Sensors and Actuators

The exoskeleton scheme integrates multi-level sensor data, physical model, and functional requirements. These coupled factors are integrated into a control system, which not only realizes local autonomy, but also integrates to realize the expression of the overall function, while avoiding one thing and the other contradictions.

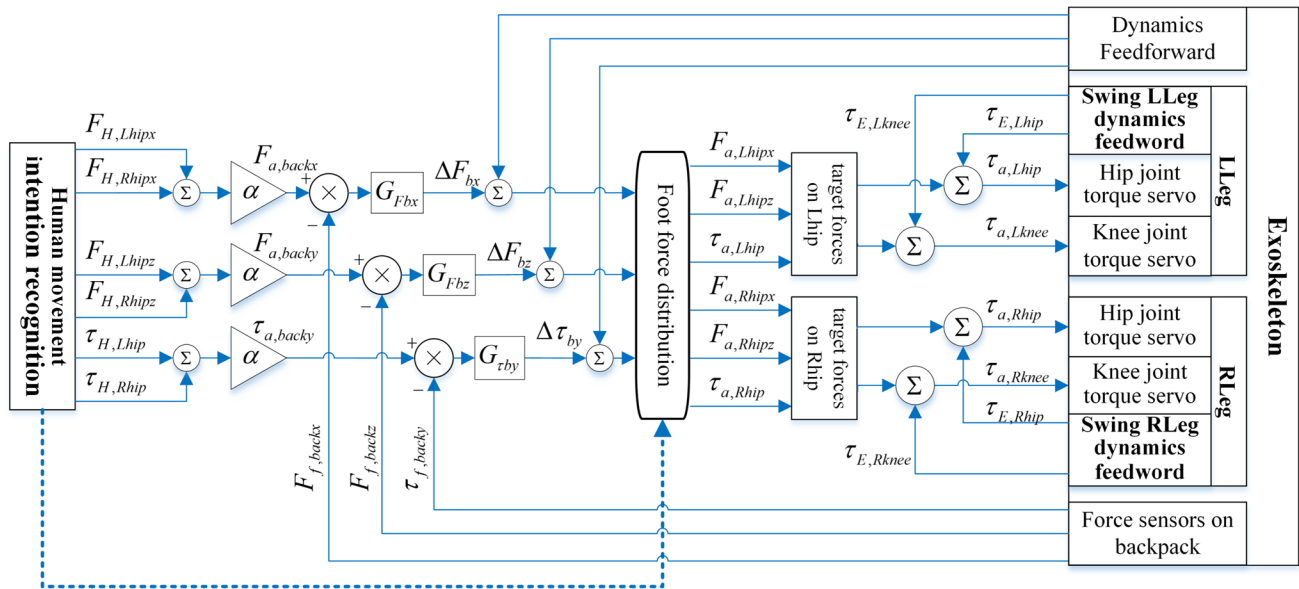


Fig. 8 Feedback compensation diagram of the support leg. The blue solid lines represent the transmission of variable information, and the blue dashed lines indicate finite state transitions

The sensor system integrated into the exoskeleton serves two primary purposes: firstly, to capture the motion information of the exoskeleton itself for dynamics feedforward and joint feedback control; secondly, through a H.-E. information coupling, to indirectly acquire information about human body locomotion. Additionally, it monitors H.-E. interaction forces information for the perception of human motion intentions and feedback control of H.-E. contact forces. The installation locations of these sensors within the exoskeleton are illustrated in [3, 10].

In this work, custom-designed integrated hydraulic drive units are employed, as depicted in Fig. 9. It utilizes pressure-flow (P-Q) valve-controlled asymmetric hydraulic cylinders as the actuators [30]. A force sensor is integrated at each piston rod end for force feedback, while parallelly arranged resistive linear displacement sensors measure the piston rod's displacement. Pressure sensors are used to acquire pressure in the two chambers. The rated pressure of the hydraulic cylinder is 18 MPa.

4 Experimental Results

Based on the requirements of the hierarchical control scheme and the joint torque servo control, several key indicators have been proposed for the control system: (1) a high sampling frequency to reduce the delay of intention recognition, (2) high computational performance to support real-time solvers and closed-loop controllers, and (3) high reliability to prevent system failures that could injure the wearers. In this work, a valve-controlled hydraulic servo system is utilized to achieve high-bandwidth force control, enabling force closed-loop control. The controller employs a high-performance PLC with a PC core that implements a 1kHz signal sampling, feedforward, and feedback loop. It allows

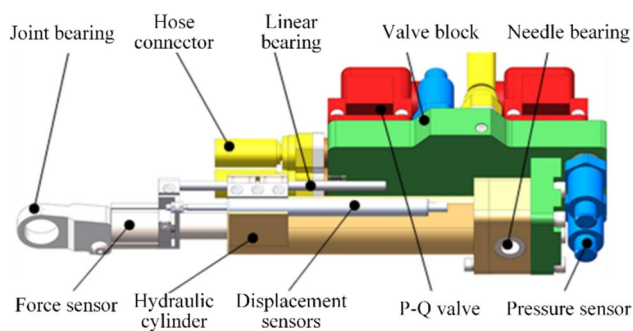


Fig. 9 Integration hydraulic driven unit for exoskeletons. The pressure sensors are employed to acquire pressure data from both chambers of the hydraulic cylinder. The linear bearing serves to prevent the rotation of the piston rod, thus preventing the failure of the displacement sensors. Additionally, the joint bearing helps prevent the piston rod from bearing radial forces that could lead to seal failure

the system to respond to force signals and reduces prediction distortion caused by sampling delays.

The hardware architecture of the hydraulic exoskeleton is depicted in Fig. 10.

An integrated overall hardware architecture is adopted in this work, with a high-performance and reliable industrial controller serving as the main controller. A/D conversion modules collect information on joint-driven hydraulic cylinder forces, displacements, pressures in both chambers, and contact forces. D/A conversion modules are used to control hydraulic valves. Serial communication is employed for the collection of IMU data, as well as for connecting with servo drives to control the motor speed and torque of the hydraulic power unit.

We demonstrate various experiments on a hydraulic exoskeleton to validate the advantages of the hierarchical control architecture we proposed. The wearer wore the exoskeleton and performed three distinct locomotion tasks: stepping, squatting, and jumping. For each movement mode, the exoskeleton was sequentially set to three modes: non-powered, follow-up, and active assistance, while experimental data was recorded. In the non-powered mode, the target torque of each driven joint of the exoskeleton was zero, and all the forces required for the exoskeleton's movement were borne by the human. In the follow-up mode, the exoskeleton activated dynamic feedforward and feedback compensation, and the target value of the H.-E. contact forces were set to zero. This meant that the exoskeleton always followed the human body's motion and tried to keep the contact force between the human and exoskeleton zero through servo control. In the active assistance mode, the exoskeleton activated intention recognition, predicted the joint torque required by the human, and applied forces to the wearer to reduce the wearer's load. In the experiment, the assistance coefficient was set to a value of 0.25. Even if there were significant errors in perceiving the motion intention, the wearer could overcome the resistance of the exoskeleton and continue moving, thus ensuring the wearer's safety.

The wearer weighed approximately 77 kg, while the exoskeleton had a weight of about 45 kg. The exoskeleton was connected to the human body only at the torso and the left and right foot ends. For analytical convenience, the backpack contact force was transferred to the hip joint, and the foot-end contact forces were transferred to the ankle joints. These forces were then projected onto the world coordinate system, as illustrated in Fig. 11. The recorded forces include the backpack contact force F_{Bz} , left foot-end contact force F_{LFz} , and right foot-end contact force F_{RFz} .

The experimental results for non-powered, follow-up, and active assistance during stepping, squatting, and jumping are depicted in Fig. 12.

In the case of the stepping task, the backpack force F_{Bz} profile indicates that the exoskeleton exerts a negative

Fig. 10 The hardware architecture of the hydraulic active power-assist exoskeleton robot. The dashed box represents various components of the exoskeleton, each of which includes corresponding sensors, valves, input/output interfaces, etc.

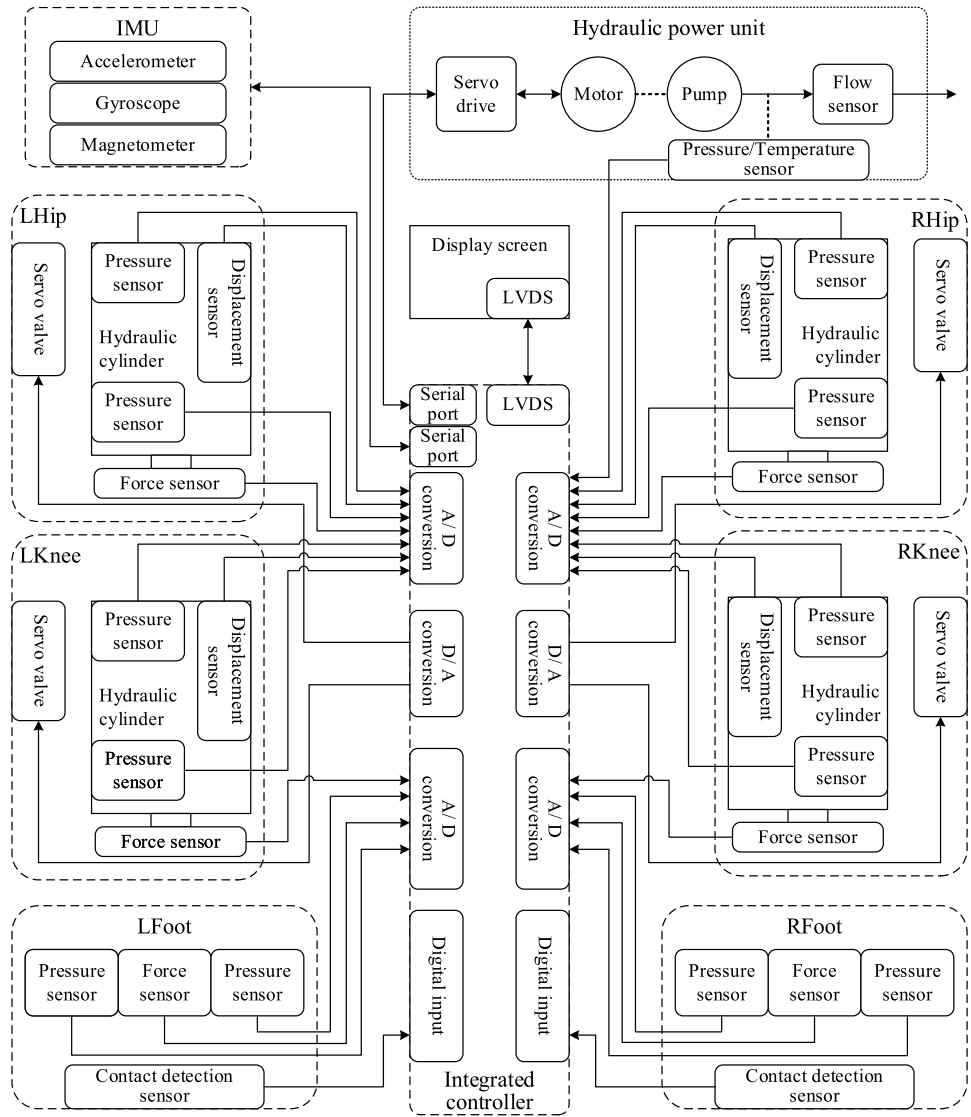


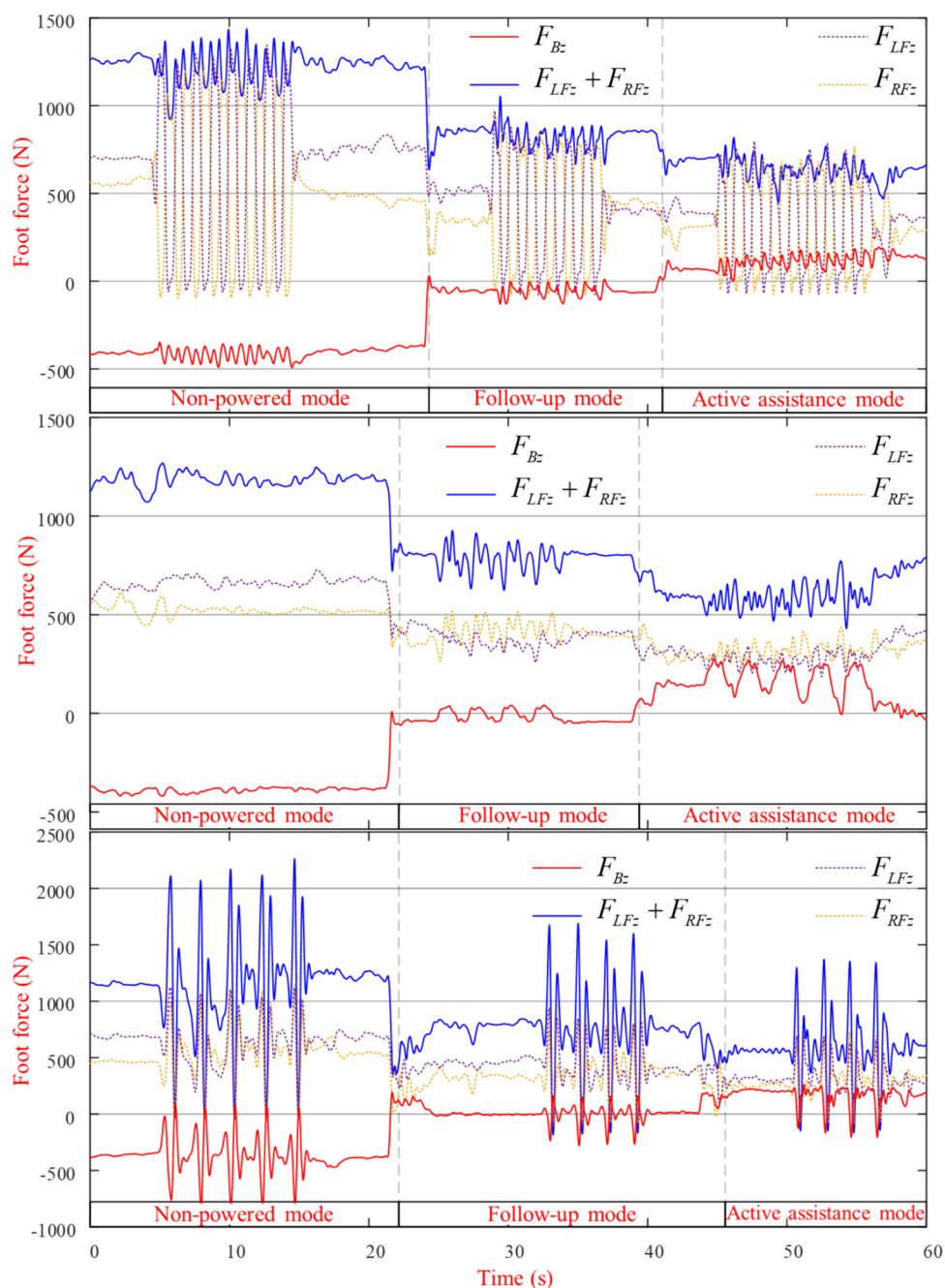
Fig. 11 Exoskeleton non-powered, follow-up, and active assistance experiments



force of approximately -410.4 N on the wearer's torso during non-powered mode. This suggests that the majority of the exoskeleton's weight is pressing on the wearer's torso, while a portion of the leg weight is transmitted to the ground through the foot-end. The left and right foot-ends contact forces F_{LFz} and F_{RFz} exhibit complementary patterns

synchronized with the stepping rhythm, with an average total foot force $F_{LFz} + F_{RFz}$ of approximately 1228.9 N , slightly less than the sum of the gravitational forces of the wearer and the exoskeleton. During the leg-raising phase, the exoskeleton applies a negative force of about -80 N on the swing leg. In the follow-up mode, the amplitude of F_{Bz} immediately

Fig. 12 Non-powered, follow-up, and active assistance results during stepping, squatting, and jumping. Shown are the three different locomotion tasks of stepping (top row), squatting (middle row), and jumping (bottom row)



decreases, with an average value of approximately -58.3N . The total foot force $F_{LFz} + F_{RFz}$ decreases to around 828.3N , and the mean swing phase foot contact force approaches 0N . This phenomenon suggests that the exoskeleton's active joints bear most of its own weight, and any residual force on the wearer may be attributed to factors such as errors in the H.-E. contact force closed-loop control. In the active assistance mode, the backpack force changes from negative to positive, reaching 111.5N , indicating that the exoskeleton is lifting the wearer. The total foot force further decreases

to around 640.2N , below the gravitational force acting on the human body.

During the squatting experiments, the force profiles exhibit similar mean values to those observed during stepping. Due to the absence of fluctuations caused by the stance and swing phase switch, the backpack force and foot force curves show smaller variations. In the non-powered mode, the mean backpack force F_{Bz} is -391.6N , and the mean total foot force $F_{LFz} + F_{RFz}$ is 1184.9N . In the follow-up mode, the mean backpack force is around -20.5N , and the mean total foot force $F_{LFz} + F_{RFz}$ decreases to approximately 790.5N . In

the active assistance mode, the backpack force changes from negative to positive, with a mean value of 142.2 N, and the total foot force further decreases to 613.7 N.

The force profiles recorded during the jumping experiments are illustrated in the bottom row of Fig. 12. During take-off, significant vertical acceleration leads to substantial loads on both the backpack and foot contacts. After takeoff, both legs are in free fall through the air, and the backpack and foot contact forces rapidly converge to zero. Upon landing, a substantial impact causes the peak foot contact force to far exceed the mean value. In the non-powered mode, the mean backpack force is - 370.6 N, with a peak near - 852.2 N, and the mean total foot force is 1163.8 N, with a peak of 2263 N, almost twice the mean. This indicates a significant impact on the human torso, resulting in the body bearing a load much higher than its weight. In the follow-up mode, the mean backpack force is - 1.6N, and the mean total foot force decreases to 771.6 N, with a peak of 1676N. In the active assistance mode, the backpack force changes from negative to positive, with a mean of 166.5 N, and the mean total foot force further decreases to 587.5 N, with a peak reduced to 1370 N, significantly lower than the 2263 N observed in the non-powered mode.

The data from three different locomotion experiments reveal consistent assistant performance in the exoskeleton, indicating that the proposed hierarchical control scheme

is applicable to the complex and varied locomotion of the human body.

To quantitatively analyze the effectiveness of the exoskeleton, the concept of angular impulse is introduced. angular impulse measures the cumulative effect of torque on a joint over time. In this paper, the angular impulse is defined as the integral of the assisting torque.

$$A_M = \int_0^T A_T dt \tag{17}$$

The statistical results of the angular impulse A_M for the assisting torque are presented in Table 1. From the data, it can be observed that, across all three motion modes, each joint (hip and knee) of the right and left legs for the five wearers obtained positive values for the angular impulse. This indicates that the exoskeleton provided positive assisting angular impulse for wearers in various locomotion.

Additionally, comprehensive terrain tests were carried out on the exoskeleton, encompassing rough terrains, ascending and descending stairs, and overcoming obstacles. The staircase steps had an approximate height of 150 mm, while the obstacles were around 500 mm in height, as shown in Fig. 13. These experiments validated the effectiveness of the proposed hierarchical control scheme.

Table 1 Auxiliary angular impulse of the hip and knee joints for both left and right legs during stepping, squatting, and jumping experiments involving 5 different participants

Wearers		Stepping		Squatting		Jumping	
		Hip	Knee	Hip	Knee	Hip	Knee
Wearer 1	LLeg A_M (kg · m ² /s)	7.0	6.6	6.9	8.7	3.5	10.4
	Weight	0.23	0.30	0.18	0.29	0.12	0.33
	RLeg A_M (kg · m ² /s)	2.3	7.8	9.4	9.2	5.5	10.1
	Weight	0.08	0.32	0.26	0.29	0.18	0.33
Wearer 2	LLeg A_M (kg · m ² /s)	9.0	11.9	2.7	9.5	4.9	10.6
	Weight	0.29	0.33	0.31	0.33	0.38	0.32
	RLeg A_M (kg · m ² /s)	8.5	11.3	4.5	10.2	5.3	10.9
	Weight	0.27	0.33	0.34	0.33	0.35	0.32
Wearer 3	LLeg A_M (kg · m ² /s)	3.6	5.6	4.3	6.3	2.4	9.4
	Weight	0.26	0.34	0.29	0.33	0.28	0.33
	RLeg A_M (kg · m ² /s)	3.2	7.2	4.2	7.5	3.0	9.3
	Weight	0.21	0.35	0.30	0.33	0.29	0.33
Wearer 4	LLeg A_M (kg · m ² /s)	3.3	3.8	7.8	11.5	4.8	9.5
	Weight	0.19	0.30	0.29	0.34	0.27	0.33
	RLeg A_M (kg · m ² /s)	2.0	4.3	11.2	10.0	5.6	8.9
	Weight	0.14	0.31	0.33	0.32	0.31	0.33
Wearer 5	LLeg A_M (kg · m ² /s)	2.0	7.0	4.8	9.8	1.7	9.2
	Weight	0.24	0.32	0.20	0.33	0.11	0.33
	RLeg A_M (kg · m ² /s)	1.9	6.1	5.4	11.4	3.0	9.4
	Weight	0.29	0.32	0.24	0.32	0.23	0.33

The weights of the auxiliary angular impulse are tabulated



Fig. 13 Active power-assist experiments in challenging terrains

5 Conclusions

This paper introduces a novel hierarchical control scheme with five sub-layers for a hydraulic active power-assist exoskeleton. The theoretical framework and functions of each layer are detailed. The proposed scheme prioritizes wearer-dominant movement, ensuring that the exoskeleton actively assists based on the wearer's motion intentions without interfering with natural body movements due to its inertia. The scheme incorporates separate modeling of the legs and backpack, along with a force distribution method, effectively addressing the challenges associated with transitions between swing and stance phases, as well as resolving statically indeterminate situations during double-foot support. Furthermore, the hierarchical control scheme exhibits active assistance capabilities during stepping, squatting, and jumping. For future work, we aim to enhance the precision of human modeling by focusing on accurate human modeling or automatic identification of human parameters, thereby improving the level of intention perception.

Acknowledgements This work was supported by the China Postdoctoral Science Foundation (No. 2020M672823), National Natural Science Foundation of China National Natural Science Foundation of China (No. 52305072, U2013602), Natural Science Foundation of Hebei Province of China (No. E2022203095), Shenzhen Science and Technology Program (No. JSGG20201102152602007), Shenzhen Science and Technology Research and Development Foundation (No. JCYJ20190813171009236), and Basic Scientific Research of Technology (No. JCKY2020603C009).

Data Availability Statement The datasets generated and analyzed during the current study are not publicly available, as the data also forms part of an ongoing study but are available from the corresponding author on reasonable request.

Declarations

Conflict of Interest The authors declare that they have no conflicts of interest relevant to the content of this article.

References

1. Qiu, S., Pei, Z. C., Wang, C., & Tang, Z. Y. (2023). Systematic review on wearable lower extremity robotic exoskeletons for assisted locomotion. *Journal of Bionic Engineering*, 20(2), 436–469.
2. Tang, X. Y., Wang, X. P., Ji, X. M., Zhou, Y. W., Yang, J., Wei, Y. C., & Zhang, W. J. (2022). A wearable lower limb exoskeleton: Reducing the energy cost of human movement. *Micromachines*, 13(6), 900.
3. Deng, J., Wang, P. F., Li, M. T., Guo, W., Zha, F. S., & Wang, X. (2017). Structure design of active power-assist lower limb exoskeleton apal robot. *Advances in Mechanical Engineering*, 9(11), 168781401773579.
4. Kong, Y. K., Choi, K. H., Cho, M. U., Kim, S. Y., Kim, M. J., Shim, J. W., Park, S. S., Kim, K. R., Seo, M. T., Chae, H. S., & Shim, H. H. (2022). Ergonomic assessment of a lower-limb exoskeleton through electromyography and Anybody modeling system. *International Journal of Environmental Research and Public Health*, 19(13), 8088.
5. Lee, H., Ferguson, P. W., & Rosen, J. (2020). Lower limb exoskeleton systems—overview. *Wearable Robotics* (pp. 207–229). Elsevier.
6. Chen, W., Li, J., Zhu, S. Y., Zhang, X. D., Men, Y. T., & Wu, H. (2022). Gait recognition for lower limb exoskeletons based on interactive information fusion. *Applied Bionics and Biomechanics*. <https://doi.org/10.1155/2022/9933018>
7. Yeung, L. F. Ockenfeld, C., Pang, M. K., Wai, H. W., Soo, O. Y., Li, S. W., Tong, K. Y. (2017). Design of an exoskeleton ankle robot for robot-assisted gait training of stroke patients. *IEEE International Conference on Rehabilitation Robotics*, London, UK (pp. 211–215).
8. Orhan, Z. Ö., Shafiee, M., Juillard, V., Oliveira, J. C., Ijspeert, A., Bouri, M. (2023). ExoRecovery: Push recovery with a lower-limb

- exoskeleton based on stepping strategy. arXiv preprint [arXiv: 2310.20339](https://arxiv.org/abs/2310.20339).
9. Chinmilli, P., Redkar, S., Zhang, W. L., & Sugar, T. (2017). A review on wearable inertial tracking based human gait analysis and control strategies of lower-limb exoskeletons. *International Robotics & Automation Journal*, 3(7), 398–415.
 10. Li, M. T., Deng, J., Zha, F. S., Qiu, S. Y., Wang, X., & Chen, F. (2018). Towards online estimation of human joint muscular torque with a lower limb exoskeleton robot. *Applied Sciences*, 8(9), 1610. <https://doi.org/10.3390/app8091610>
 11. Qian, Y. P., Wang, Y. N., Chen, C. H., Xiong, J. F., Leng, Y. Q., Yu, H. Y., & Fu, C. L. (2022). Predictive locomotion mode recognition and accurate gait phase estimation for hip exoskeleton on various terrains. *IEEE Robotics and Automation Letters*, 7(3), 6439–6446.
 12. Qian, Y. P., Wang, Y. N., Geng, H. L., Du, H., Xiong, J. F., Leng, Y. Q., & Fu, C. L. (2023). Adaptive oscillator-based gait feature extraction method of hip exoskeleton for stroke patients. *IEEE Transactions on Medical Robotics and Bionics*. <https://doi.org/10.1109/TMRB.2023.3329585>
 13. Choi, S., Ko, C., & Kong, K. (2023). Walking-speed-adaptive gait phase estimation for wearable robots. *Sensors*, 23(19), 8276. <https://doi.org/10.3390/s23198276>
 14. Sun, Y. X., Tang, Y. T., Zheng, J., Dong, D. B., Chen, X. H., & Bai, L. (2022). From sensing to control of lower limb exoskeleton: A systematic review. *Annual Reviews in Control*, 53, 83–96.
 15. Li, K. X., Zhang, J. H., Wang, L. F., Zhang, M. L., Li, J. Y., & Bao, S. C. (2020). A review of the key technologies for semg-based human-robot interaction systems. *Biomedical Signal Processing and Control*, 62(11), 102074. <https://doi.org/10.1016/j.bspc.2020.102074>
 16. Asanza, V., Peláez, E., Loayza, F., Lorente-Leyva, L. L., & Peluffo-Ordóñez, D. H. (2022). Identification of lower-limb motor tasks via brain–computer interfaces: A topical overview. *Sensors*, 22(5), 2028. <https://doi.org/10.3390/s22052028>
 17. Li, M. Y., Duan, S. C., Dong, Y., Wang, C., Feng, W., Wu, X. (2020). A hierarchical fusion strategy based on EEG and sEMG for human-exoskeleton system. In *2020 IEEE International Conference on Real-time Computing and Robotics (RCAR)*. Asahikawa, Japan, (pp. 458–463).
 18. Tortora, S., Tonin, L., Chisari, C., Micera, S., & Artoni, F. (2020). Hybrid human-machine interface for gait decoding through bayesian fusion of EEG and EMG classifiers. *Frontiers in Neurobotics*, 14, 582728. <https://doi.org/10.3389/fnbot.2020.582728>
 19. Shi, K. C., Huang, R., Mu, F. J., Peng, Z. N., Huang, K., Qin, Y. Z., Yang, X. Cheng, H. (2022). A novel multimodal human-exoskeleton interface based on EEG and sEMG activity for rehabilitation training. In *2022 International Conference on Robotics and Automation (ICRA)*, Philadelphia, PA, USA (pp. 8076–8082).
 20. Nasr, A., Hunter, J., Dickerson, C. R., & McPhee, J. (2023). Evaluation of a machine-learning-driven active–passive upper-limb exoskeleton robot: Experimental human-in-the-loop study. *Wearable Technologies*, 4, e13. <https://doi.org/10.1017/wtc.2023.9>
 21. Masengo, G., Zhang, X. D., Dong, R. L., Alhassan, A. B., Hamza, K., & Mudaheerawa, E. (2023). Lower limb exoskeleton robot and its cooperative control: A review, trends, and challenges for future research. *Frontiers in Neurobotics*, 16, 913748. <https://doi.org/10.3389/fnbot.2022.913748>
 22. Wang, J. Q., Wu, D. M., Gao, Y. Z., Wang, X. R., Li, X. Q., Xu, G. Q., & Dong, W. (2022). Integral real-time locomotion mode recognition based on GA-CNN for lower limb exoskeleton. *Journal of Bionic Engineering*, 19(5), 1359–1373.
 23. Liu, K. P., Li, L., Li, W. T., Gu, J., & Sun, Z. B. (2023). Compliant control of lower limb rehabilitation exoskeleton robot based on flexible transmission. *Journal of Bionic Engineering*, 20(3), 1021–1035.
 24. Laubscher, C. A., Goo, A., Farris, R. J., & Sawicki, J. T. (2022). Hybrid impedance-sliding mode switching control of the indego explorer lower-limb exoskeleton in able-bodied walking. *Journal of Intelligent & Robotic Systems*, 104(4), 76. <https://doi.org/10.1007/s10846-022-01583-7>
 25. Liu, L., Illian, M., Leonhardt, S., & Misgeld, B. (2023). Iterative learning control for cascaded impedance-controlled compliant exoskeleton with adaptive reaction to spasticity. *IEEE Transactions on Instrumentation and Measurement*, 72, 1–11.
 26. Sun, Y. H., Peng, Z. N., Hu, J. P., & Ghosh, B. K. (2024). Event-triggered critic learning impedance control of lower limb exoskeleton robots in interactive environments. *Neurocomputing*, 564, 126963.
 27. Yang, Y., Huang, D. Q., Jin, C. W., Liu, X., & Li, Y. N. (2023). Neural learning impedance control of lower limb rehabilitation exoskeleton with flexible joints in the presence of input constraints. *International Journal of Robust and Nonlinear Control*, 33(7), 4191–4209.
 28. Nasr, A., Hashemi, A., & McPhee, J. (2022). Model-based mid-level regulation for assist-as-needed hierarchical control of wearable robots: A computational study of human-robot adaptation. *Robotics*, 11(1), 20. <https://doi.org/10.3390/robotics11010020>
 29. Neilson, P. D., & Neilson, M. D. (2005). An overview of adaptive model theory: Solving the problems of redundancy, resources, and nonlinear interactions in human movement control. *Journal of neural engineering*, 2(3), S279. <https://doi.org/10.1088/1741-2560/2/3/S10>
 30. Shi, Y. P., Li, M. T., Zha, F. S., Sun, L. N., Guo, W., Ma, C., & Li, Z. B. (2020). Force-controlled compensation scheme for P-Q valve-controlled asymmetric cylinder used on hydraulic quadruped robots. *Journal of Bionic Engineering*, 17(6), 1139–1151.

Publisher's Note Springer Nature remains neutral with regard to jurisdictional claims in published maps and institutional affiliations.

Springer Nature or its licensor (e.g. a society or other partner) holds exclusive rights to this article under a publishing agreement with the author(s) or other rightsholder(s); author self-archiving of the accepted manuscript version of this article is solely governed by the terms of such publishing agreement and applicable law.